Environ. Sci. Technol. **2006**, *40,* 5490−5495

Biological Reduction of Nanoengineered Iron(III) Oxide Sculptured Thin Films

HUI TAN,[†] OBIEFUNE K. EZEKOYE,[‡] JAMES VAN DER SCHALIE,[†] MARK W. HORN,[‡] AKHLESH LAKHTAKIA,[‡] JIAN XU,[‡] AND WILLIAM D. BURGOS*[,†]

Department of Civil and Environmental Engineering, 212 Sackett Building, The Pennsylvania State University, University Park, Pennsylvania 16802-1408, and Department of Engineering Science and Mechanics, The Pennsylvania State University, University Park, Pennsylvania

Sculptured thin films (STFs) are assemblies of nominally identical, parallel nanowires with tailored shapes such as chevrons and spirals. A series of iron(III) STFs were produced with varied crystallinity (from hematite to ferrihydrite) and nanowire shapes (slanted columnar, clockwise helical, and counterclockwise helical). When the dissimilatory metal-reducing bacterium *Shewanella putrefaciens* CN32 was used to measure their bioreducibility, it was found that bioreduction was controlled primarily by oxide crystallinity. STFs were characterized by scanning electron microscopy, atomic force microscopy, and grazing incidence small-angle X-ray scattering. Postbioreduction characterizations determined that mineralogy of the film materials did not change, but surface roughness generally increased. Changes caused by bioreduction were assessed in terms of both transmittance and reflectance of light incident normal to the STFs. The greatest optical changes were obtained with crystalline hematite films. These results underscore the feasibility of an STF-based fiber optic iron(III) reduction sensor for in situ subsurface deployment.

Introduction

Because of their redox activity and abundance in soils, solid-phase iron(III) (oxyhydr)oxides are important electron acceptors in anaerobic subsurface environments. A developing technology for the in situ treatment of contaminated soil and groundwater is the stimulation of dissimilatory metal-reducing bacteria (DMRB) (*1*). A variety of reducible inorganic (e.g., Cr(VI), Tc(VII), and U(VI)) and organic contaminants (e.g., chlorinated solvents and trinitrotoluene) can be either directly reduced by DMRB or indirectly reduced by biogenic Fe(II) (*2*−*5*). DMRB activity can be stimulated by the addition of a nonfermentable electron donor (e.g., acetate) to a contaminated zone to promote the activity of native DMRB over other species in the subsurface microbial community. An Fe(II) enriched reactive zone could then be created to intercept and treat contaminated groundwater.

Since the stimulation of iron(III) reduction is an important outcome from electron-donor addition (assuming that contaminant reduction would parallel this process), monitoring the reduction of iron(III) with an in situ real-time sensor would be a significant improvement over the current procedure comprising groundwater purging, sampling, and laboratory analysis (*6*). Field-scale treatability studies using wells equipped with such sensors could be conducted rapidly under site-specific conditions (a) representing soil consolidation, temperature, pressure, and groundwater chemistry and (b) employing the indigenous microbial community. In addition, assuming such sensors would be robust enough to last for months in the subsurface, sensors could be buried or driven to depth outside of a well screen and used for the long-term monitoring of a biostimulation experiment. Such a sensor would directly reveal when iron(III)-reducing conditions are established and indirectly measure the redox condition surrounding the sensor. A fiber optic-based sensor system using a sculptured thin film of iron(III) oxide could be designed and fabricated for this purpose, as discussed in the final section of this manuscript.

Sculptured thin films (STFs) are nanoengineered materials containing nominally identical, parallel nanowires of tailored shapes grown on a substrate using physical vapor deposition (*7*). The nanowires are made of 1−3 nm clusters and are 50−300 nm in diameter. Their shapes can range from simple slanted or upright columns to zigzags and S's to helices as well as combinations thereof to produce a wide range of nanomorphologies. STFs can be produced from virtually any material that can be evaporated including inorganics such as silicon oxide and magnesium fluoride, metals, and even organic polymers such as parylene (*8*). The substrates can be either flat or have lithographically defined topography at the micron or submicron scales (*9*, *10*). Surface lithography is expected to provide great flexibility in designing STF morphology for specific purposes by blending the micro- and the nanoscales. Most importantly for the present purposes, a large variety of optical devices can be made of STFs (*7*), and their porosity has already been demonstrated experimentally to be of significance for chemical sensing through a dynamic modification of the optical response characteristics (*11*).

A significant amount of current research is focused on DMRB-promoted in situ iron(III) and concomitant contaminant reduction (e.g., refs *12*). This research effort could be advanced with the development of robust, field-deployable sensor systems. The use of nanoengineered materials represents a natural merging of the scientific areas of nanomaterials and biogeochemistry into the emerging field of nanobiogeosciences (*13*, *14*). Our initial objectives were to (1) manufacture a series of iron(III) STFs of varied crystallinity and nanowire shape, (2) measure the bioreducibility of these materials using a DMRB pure culture, and (3) characterize changes in optical properties of iron(III) STFs caused by biological reduction.

Experimental Section

The STFs chosen for the reported research may be classified based on deposition technique (evaporated or sputtered) and nanowire shape (slanted columnar, clockwise helical, or counterclockwise helical). The substrates used in this experiment were low-alkali Corning 7059 glass and silicon crystal precut into 0.25-in. × 0.50-in. pieces. The 7059 glass was selected because of its low optical absorption and high transmission across visible wavelengths. The silicon substrates were primarily selected for structural and mineralogical characterization. Before deposition, the substrates were prepared by a cleaning sequence of acetone, isopropyl alcohol, and deionized water. After cleaning, the substrates

* Corresponding author phone: (814)863-0578; fax: (814)863-7304; e-mail: wdb3@psu.edu.
[†] Department of Civil and Environmental Engineering.
[‡] Department of Engineering Science and Mechanics.

10.1021/es060388j CCC: $33.50

Published on Web 08/03/2006

were blown dry with compressed air and placed into the deposition chamber. For both sputter and evaporation depositions, 12 glass and 6 silicon substrates were mounted onto a stepper motor apparatus that was constructed for in situ control of rotation about axes both parallel and perpendicular to the substrate surface. In this work, the incident flux angle was fixed at 80 degrees to the substrate plane. Evaporated STFs (*7*) were produced by electron-beam evaporation of 99.95% pure metallic iron(0) pieces obtained from Kurt J. Lesker Co. Graphite crucibles (100 cm^3) were used to hold the source material during evaporation. For all depositions, the base pressure was between ca. 5×10^{-6} and 2×10^{-5} Torr, and all depositions began at room temperature, ca. 23 °C. The substrate−crucible distance was 17.5 cm. No additional gas was introduced into the deposition environment. The rotation speed (about the helical axis) for both the counterclockwise and the clockwise STFs was 1.5 revolutions/min. Film thickness was measured using a Tencor P-10 contact profilometer. The nominal deposition rate was measured by dividing the measured film thickness by the total deposition time. For evaporated films, the nominal deposition rate was 11.5 Å/s. Evaporated iron(0) STFs were oxidized to iron(III) in a 500 °C furnace flushed with pure oxygen for 15 h.

Sputtered STFs (*7*) were produced using radio frequency (RF) heating of an α-Fe_2O_3 target. The base pressure for the chamber was between 1×10^{-6} and 5×10^{-5} Torr, and pure Ar was used as the sputtering gas at ca. 7.5×10^{-3} Torr. For all depositions, the net power sent to the plasma source was 100 W. The distance between the target and the substrate holder was 7.0 cm. Sputtered STF nanowire shapes were slanted columnar, clockwise helical, or counterclockwise helical. For helical films, the rotation speed was 0.057 revolutions/min. The nominal deposition rate for the sputtered films was 0.185 Å/s. Sputtered STFs were also annealed in a 500 °C furnace flushed with pure oxygen for 15 h.

STFs were characterized by scanning electron microscopy (SEM), atomic force microscopy (AFM), grazing incidence small-angle X-ray scattering (GISAXS), and optical transmittance and reflectance. A LEO 1530 field emission-SEM was used for cross-section imaging of the STFs to confirm nanowire shape. A BioScope AFM (Digital Instrument, Santa Barbara, CA) with silicon nitride AFM tips and a Nanoscope IIIa control system was used in contact mode to measure surface roughness. The grazing incidence geometry of GISAXS has advantages over conventional X-ray diffractometry for the crystallographic and structural analysis of thin films and other nanoscale surface features (*15*, *16*) due to the fact that a small incidence angle increases the path length of the incident beam through the film, that simultaneously yields a stronger signal from the film and minimizes large peaks contributed by the film substrate (*17*, *18*). The unit used in this study was a Scintag-X2 with a θ/θ goniometer and a Cu tube emitting Kα1/Kα2 X-rays. The grazing angle used was 2°, and the scan was from 10° to 64° with 2-θ at 2° per min.

Optical transmittance and reflectance data were collected on both bioreduced STFs and abiotic control STFs. All measurements were conducted with the light passing through the center of the sample. For collection of transmittance spectra, light emitted by a xenon bulb was released through a fiber optic cable, passed through a neutral density filter and a focusing lens, cropped to a 5 mm-diameter circular beam with an iris, and passed through the sample to an Ocean Optics HR 2000 high-resolution spectrometer. For collection of reflectance spectra, the same light source, filter, lens, and iris were used to create a 5 mm-diameter circular beam, and the light was then passed through a nonpolarized beam splitter (50−50%) to pass the light reflected back from the sample to the spectrometer.

Shewanella putrefaciens strain CN32 (referred to as CN32) was grown aerobically on tryptic soy broth without dextrose at 20 °C on an orbital shaker (100 rpm) (*19*). Cells were harvested by centrifuging (3500*g*, 10 min, 15 °C) from a 16-h-old culture and washed three times in 10 mM 1,4-piperazinediethanosulfonic acid (PIPES, pH 6.8), the final wash being made with deoxygenated solution. Cell pellets were resuspended in anoxic PIPES, and cell density was determined by optical-absorbance measurement at 420 nm wavelength and adjusted to 1×10^9 cells mL^{-1} CN32. Experiments were conducted in 20-mL glass serum bottles containing 10 mL of a 10 mM PIPES plus 1.5 mM ferrozine solution (total final volume and concentrations). Ferrozine, an Fe(II) complexant, was used to keep biogenic Fe(II) in solution and provided a colorimetric indicator of reduction extent. All preparations were performed in an anaerobic chamber (Coy, Grass Lakes, MI). Bioreduction experiments were started by adding 1.0 mL of 1×10^9 cells mL^{-1} CN32 to 9.0 mL of buffer (final cell concentration of 1×10^8 cells mL^{-1}; resting cell conditions) that included one 0.25-in. × 0.50-in. STF piece as the sole electron acceptor. Hydrogen from the headspace (97.5:2.5% N_2:H_2) was the sole electron donor, and serum bottles were sealed with Teflon-faced rubber stoppers and Al crimp tops. Serum bottles were laid on their side and incubated statically at room temperature (20−22 °C). Abiotic (no-cells) controls were prepared in parallel with all experiments, and all systems were prepared with 2−5 replicates.

Experiments were designed to reach a bioreduction extent of 5−50 μM total biogenic Fe(II) evolved from the STFs. This endpoint was selected because it ensured that no more than 50% of any of the STFs were dissolved, thereby leaving enough film material for postbioreduction characterizations. In these experiments, this endpoint was reached after a 96-h incubation period. Samples were collected from the serum bottles using sterile needles, filtered (0.2-μm, cellulose acetate), and used to measure Fe(II) and pH. Filtrate samples were diluted into ferrozine reagent (1.0 g L^{-1} ferrozine in 50 mM HEPES, pH 8.0), and Fe(II) was measured by absorbance at 562 nm. Filtrate pH was measured by combination electrode in the anaerobic chamber. Serum bottles were opened to remove STF pieces which were rinsed with anoxic MilliQ water and allowed to dry in the anaerobic chamber prior to the characterization procedures described above.

Results and Discussion

Cross-sectional SEM images of the different STFs confirmed that the desired nanowire shapes were produced. Examples are presented in Figure 1. AFM images provided complementary information on film-surface topography and quantitative measurements of surface roughness of bioreduced STFs and abiotic controls (Table 1). AFM images showed that the emergent tops of individual nanowires ranged from 100 to 200 nm (Figure S1, Supporting Information). Grazing incidence small-angle X-ray scattering (GISAXS) patterns showed that all evaporated STFs, regardless of nanowire shape, were crystalline hematite, whereas the mineralogy of the sputtered STFs depended on the nanowire shape (Figure 2). Based on theoretical calculations, the X-ray penetration depth in GISAXS is very sensitive to the assumed porosity of the film (*20*, *21*). For example, at a grazing angle of 2°, X-ray penetration depths into hematite thin films would be 0.31 μm, 0.61 μm, and 1.02 μm, respectively, for films of 0%, 50%, and 70% porosity. The porosity of these films was not directly measured, but an assumed value of ca. 50% is quite reasonable. This type of analysis reveals that GISAXS most likely probed the bulk of the film materials versus the uppermost surface layer.

Furnace annealing of sputtered slanted columnar STFs (not shown) and counterclockwise helical STFs yielded

TABLE 1. Summary of Physical and Mineralogical Characterizations of Iron(III) STFs Tested

deposition technique	nanowire shape[a]	film thickness[b] (μM)	mineralogy[c]	surface roughness before bioreduction[d]	surface roughness after bioreduction[d]
evaporated	clockwise helical	0.50	hematite	9.80 ± 1.35	13.2 ± 1.95
evaporated	counterclockwise helical	0.60	hematite	4.47 ± 1.67	6.22 ± 1.84
sputtered	clockwise helical	0.82	mixture of hematite and ferrihydrite	5.10 ± 0.01	3.94 ± 1.66
sputtered	counterclockwise helical	1.15	ferrihydrite	3.78 ± 1.37	12.0 ± 1.46
sputtered	slanted columnar	1.10	ferrihydrite	N/A	N/A

[a] Designed by control of substrate stepper motors and confirmed by cross-sectional scanning electron microscopy. [b] Determined by contact profilometry. [c] Determined by grazing incidence small-angle X-ray scattering. [d] Determined by atomic force microscopy where surface roughness $R_a = 1/n\sum_{j=1}^{n}|Z_j|$, R_a is the average roughness (nm), n is the total number of data points in the image, and Z_j is the vertical distance between a data point and the mean plane (nm).

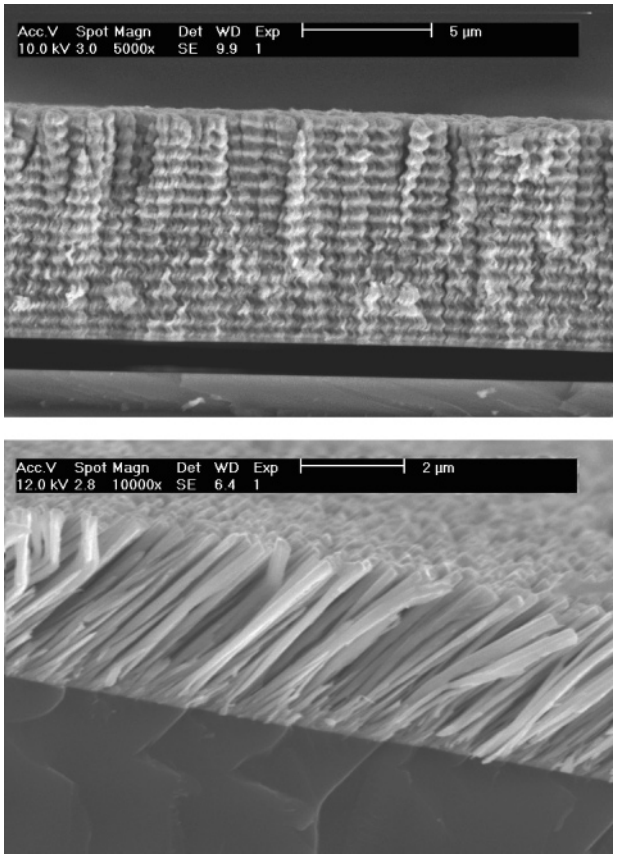

FIGURE 1. Cross-sectional SEM images of evaporated iron(0) STFs before furnace annealing: (A) 10-μm thick STF composed of clockwise helical nanowires and (B) 4-μm thick STF composed of slanted columnar nanowires.

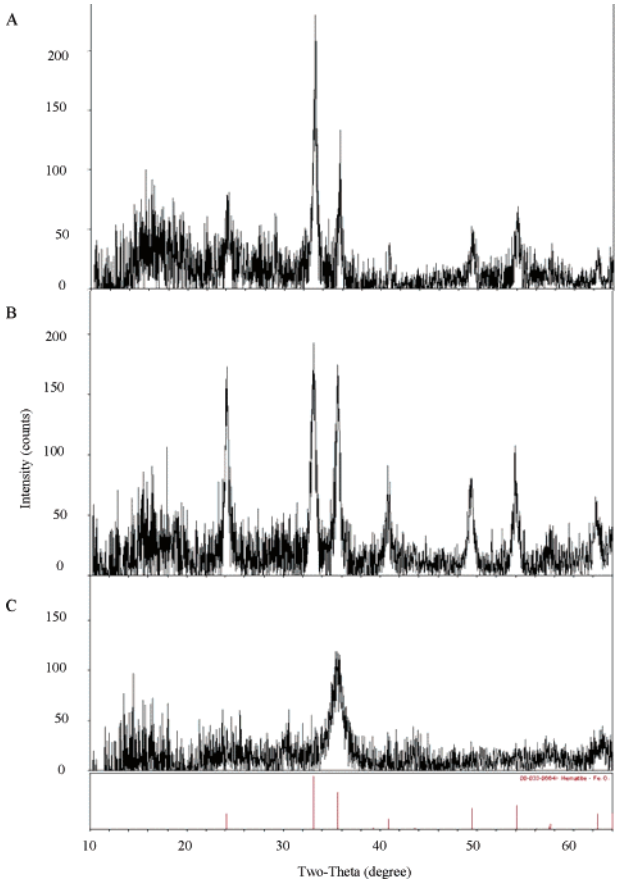

FIGURE 2. Grazing incidence small-angle X-ray scattering patterns from three of the iron(III) STFs produced and tested. Deposition technique and nanowire shape: (A) evaporated clockwise helical, (B) sputtered clockwise helical, and (C) sputtered counterclockwise helical. Reference pattern for hematite (α-Fe_2O_3).

"poorly crystalline" ferric oxide, here referred to as ferrihydrite. Furnace annealing of sputtered clockwise helical STFs yielded ferric oxide material of "intermediate" crystallinity, likely a mixture of hematite and amorphous ferrihydrite. We refer to this material as "intermediate" in crystallinity because preliminary GISAXS patterns collected at a dwell time (signal collection time at each 0.02° step) of 0.5 s showed no crystalline patterns (Figure S2, Supporting Information). When the GISAXS dwell time was increased to 12 s per 0.02° step, as for all patterns shown in Figure 2, crystalline peaks were revealed. We suspect that variations in the nanocolumn growth rate may have led to the preferential crystallization of sputtered clockwise helical STFs through furnace annealing. For example, while stepper motor controls were identical, counterclockwise helical films systematically grew to greater thicknesses compared to clockwise helical films (Table 1). This would be consistent with Okamoto et al. (*22*) who showed that the evaporation rate of obliquely deposited iron oxide thin films affected a variety of film properties, notably column angle, columnar spacing, film texture (the crystallographic direction parallel to the texture axis as well as the crystallographic plane parallel to the incident plane), and magnetic properties.

S. putrefaciens CN32 was able to bioreduce all of the iron(III) STFs tested, and STF crystallinity had a significant effect on bioreducibility (Figure 3). In all experiments, a single 0.25-in. × 0.50-in. STF piece was added to each serum bottle. While the different film types varied in film thickness (Table 1) up to a factor of 2.3 (1.15 μm thick sputtered counterclockwise helical film vs 0.50 μm thick evaporated clockwise helical film), bioreduction extents varied by a corresponding factor of 8.5. While the different film types may have varied in surface area (not directly measured in the current study), surface roughness values measured by AFM varied by a

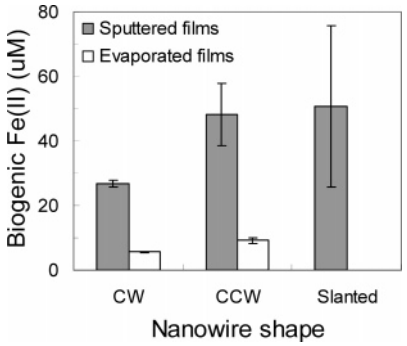

FIGURE 3. Bioreduction extent of several iron(III) STFs after 96 h incubation with *S. putrefaciens* CN32. CW and CCW refer to clockwise and counterclockwise helical nanowire shapes, respectively, and slanted refers to slanted columnar nanomorphology. All experiments were conducted with 1 × 10^8 cells mL^{-1} CN32 and 2.5% H_2(g) in a 10 mM PIPES buffer, pH 6.8, 20−22 °C. Symbols represent mean values of 2−5 replicate measurements, and error bars represent 1 SD. Fe(II) evolved from abiotic controls are not shown but never exceeded 0.9 μM.

corresponding factor of 0.38 (i.e., the less bioreduced evaporated clockwise helical film had a greater surface roughness that arguably could have compensated for the initial lower mass of Fe(III); Table 1). Evaporated STFs were the most crystalline material and bioreduced to the least extent. Sputtered slanted columnar and counterclockwise helical STFs were the least crystalline materials and bioreduced to the greatest extent. Sputtered clockwise helical STFs were intermediate with respect to both crystallinity and bioreduction extent. These results are consistent with several studies that have shown that amorphous ferric (hydr)oxides are bioreduced to a far greater extent than crystalline ferric oxides such as goethite and hematite (*23*−*25*). Filtrate pH measured at the end of all experiments ranged from pH 6.74 to 6.87. For all of the STFs tested, postbioreduction characterizations determined that mineralogy of the film materials did not change but surface roughness did change (Table 1).

Optical characterizations of bioreduced STFs versus corresponding abiotic controls showed varying degrees of change. The most substantial changes in reflectance and transmittance spectra occurred with the most crystalline evaporated STFs (Figure 4). The interference maxima and minima exhibited noticeable blue-shifts in both the reflectance and transmittance spectra, and this was highly reproducible in the replicate bioreduced STFs. Dissolution of the films, conceivably as thinning the diameters of individual nanowires, is expected to change optical-response properties—most likely as a blue-shift of spectral signatures according to a simple model of the optical properties of STFs in sensor applications (*26*). The Bragg reflection signature of uniformly helical STFs, however, was not recognizable in the reflectance and transmittance spectra, and, as a result, spectral shifts are not unambiguously identifiable in Figure 4. Nonetheless, it is clear that changes in the optical response properties of the iron(III) STFs can be predictable and exploitable for a sensor system when STF production controls are improved.

Optical-response changes caused by bioreduction were less substantial, although not negligible, for the less crystalline STFs (Figure 5). The least crystalline STFs, such as sputtered slanted columnar STFs, displayed the least systematic changes in reflectance. Sputtered clockwise helical STFs were intermediate with respect to both crystallinity and changes in reflectance. These results demonstrate that crystalline iron(III) STFs composed of helical nanowires would likely be best for sensing applications.

Potential Application for an in Situ Sensor. The importance of monitoring iron(III) reduction is that iron(III) is

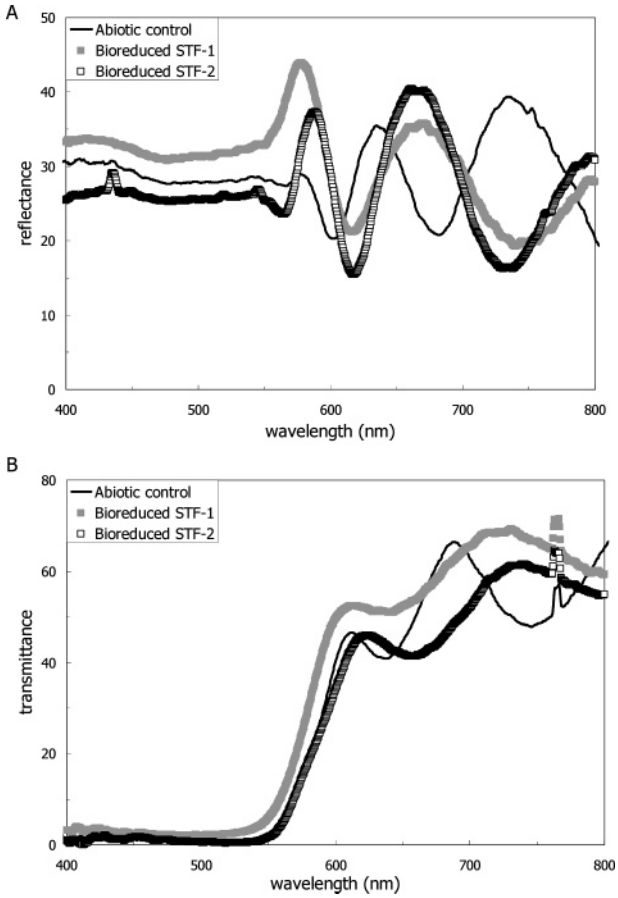

FIGURE 4. (A) Optical reflectance and (B) transmittance spectra collected from two evaporated clockwise helical iron(III) STFs that were bioreduced and one abiotic control. Film material was crystalline hematite. STF-1 and STF-2 in each panel refer to replicate film pieces.

typically the most abundant electron acceptor and most important redox buffer in subsurface environments. Monitoring chemical conditions (e.g., redox status) of subsurface sediments and groundwater is difficult. Well purging is the standard practice prior to collection of groundwater samples, because it is assumed that the well bore is a different environment than the pore space in the adjacent sediment (*6*). Water chemistry monitoring equipment for down-well deployment (e.g., pH, DO, Eh meters) is commercially available; however, Eh probes require frequent aboveground calibration and can be unreliable. In addition, groundwater sampling does not provide any direct measure of solid-phase reactions, e.g., increasing dissolved Fe(II) concentrations implies that solid-phase Fe(III) minerals are being reduced but not does not reflect the extent of loss and/or transformations of Fe(III) minerals. A design objective of our proposed STF-based optical sensor would be to create an inexpensive device that would be robust enough to last for weeks or months in the subsurface and be permanently buried at a depth inside or outside of the well screen.

This study suggests the viability of an STF-based fiber optic iron(III) reduction sensor for in situ deployment (down-well or driven and buried). The schematic of a proposed fiber optic-based sensor system is presented in Figure 6 and shows a fiber optic bundle in a centered hexagonal configuration, sensor housing, polarization optics, and STF sensing elements. The central optical fiber in the bundle would be used to transmit the incident optical beam, and the surrounding six fibers would be used to collect the Bragg reflection signal for spectrum analysis. A linear polarizer and a micromachined Fresnel Rhomb phase retarder would be

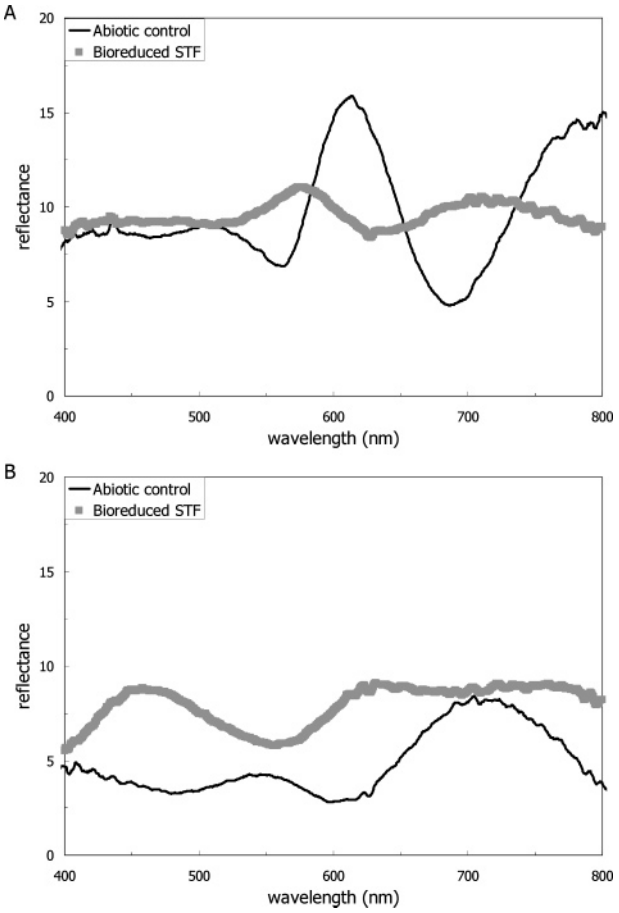

FIGURE 5. Optical reflectance spectra collected from two sputtered iron(III) STFs. (A) Sputtered clockwise helical STF was a mixture of hematite and amorphous ferrihydrite. (B) Sputtered slanted columnar STF was ferrihydrite.

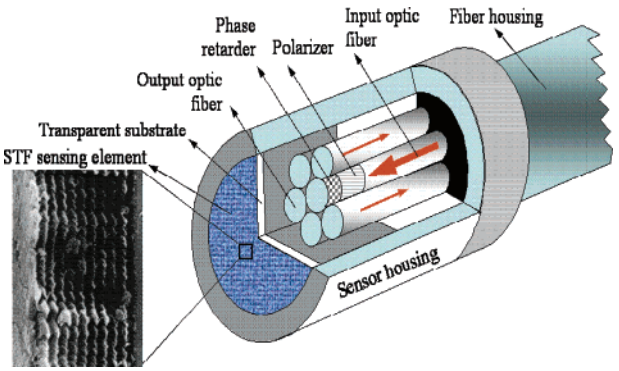

FIGURE 6. Conceptualization of an STF-based fiber optic iron(III) reduction sensor designed for in situ subsurface deployment. The reflectance sensor schematic shows the fiber optic bundle, sensor housing, polarization optics, and STF sensing elements.

installed at the end of the central optical fiber to convert the incident light to a circularly polarized beam over the fiber-transmission bandwidth. The optical fibers would be assembled in a tubular housing, whose end would be attached to a transparent substrate deposited with iron(III) oxide STFs. The Bragg reflection regime would be determined by illuminating the STF and collecting the reflected signals through the optical fiber bundle and analyzing the reflection spectrum. Subsequent changes in the material constituents and cross-sectional radius of the STF columns (due to bioreduction) would shift the sharp edges of the Bragg regime. Large variations in the Bragg reflection intensities at the wavelengths close to those edges can be viewed as a "signal amplification" process. Theoretical calculations have shown a 10% decrease of the STF column radius resulting in a large blue-shift of the Bragg reflection regime by 55 nm, which is twice the full width at half-maximum of the Bragg reflection regime itself (*26*).

The proposed sensor would exploit the Bragg phenomenon that arises in response to distributed scattering from multiple periods inside a chiral STF. There are several advantages to monitoring optical properties that are *internal* to the sensing element. First, only the sensing element would be exposed to the surrounding water-saturated environment, and all device components would be internally housed. Second, the internal optical signal would not be affected or masked by local surface reactions. For example, in some situations where the redox cycles of Fe(II/III) and reducible contaminants are strongly coupled, the reductive dissolution of Fe(III) may be effectively masked by its reprecipitation or by sorption of Fe(II). However, the optical signal in the proposed sensor will change due to loss of structural Fe(III) regardless of its reprecipitation. Similarly, biofilm formation and/or mineral precipitate formation on the sensing element would not significantly adversely affect the sensor's function. In addition, the sensor could detect solid-state conversions (e.g., ferrihydrite to magnetite) promoted by the sorption of biogenic Fe(II). Considerable advances in nanomaterials and biogeochemistry could be made through the development (i.e., design, fabrication, calibration, and in situ demonstration) of the proposed sensor.

Acknowledgments

This research was partially supported by the Natural and Accelerated Bioremediation Research Program (NABIR), Office of Biological and Environmental Research (OBER), Office of Energy Research, U.S. Department of Energy (DOE) through Grant No. DE-FG02-01ER63180 to The Pennsylvania State University, by the Penn State Center for Environmental Chemistry and Geochemistry (CECG), and by a Penn State College of Engineering Graduate Fellowship to H. Tan. Helpful discussions with Philip Long and comments from three anonymous reviewers greatly contributed to an improved presentation of our work.

Supporting Information Available

Atomic force microscope images of iron(III) STFs after abiotic incubation (Figure S1) and grazing incidence small-angle X-ray scattering patterns from a sputtered clockwise helical iron(III) STF at different X-ray dwell times (Figure S2). This material is available free of charge via the Internet at http://pubs.acs.org.

Literature Cited

(1) Lovley, D. R. Microbial Fe(III) reduction in subsurface environments. *FEMS Microbiol. Rev.* **1997**, *20*, 305−313.

(2) Wielinga, B.; Mizuba, M. M.; Hansel, C. M.; Fendorf, S. Iron promoted reduction of chromate by dissimilatory iron-reducing bacteria. *Environ. Sci. Technol.* **2001**, *35*, 522−527.

(3) Gerlach, R.; Cunningham, A. B.; Caccavo, F., Jr. Dissimilatory iron-reducing bacteria can influence the reduction of carbon tetrachloride by iron metal. *Environ. Sci. Technol.* **2000**, *34*, 2461−2464.

(4) Fredrickson, J. K.; Zachara, J. M.; Kennedy, D. W.; Kukkadapu, R. K.; McKinley, J. P.; Heald, S. M.; Liu C. X.; Plymale A. E. Reduction of TcO_4^- by sediment-associated biogenic Fe(II). *Geochim. Cosmochim. Acta* **2004**, *68*, 3171−3187.

(5) Borch, T.; Inskeep, W. P.; Harwood: J. A.; Gerlach, R. Impact of ferrihydrite and anthraquinone-2,6-disulfonate on the reductive transformation of 2,4,6-trinitrotoluene by a gram-positive fermenting bacterium. *Environ. Sci. Technol.* **2005**, *39*, 7126−7133.

(6) EPA. *Ground Water Sampling - A Workshop Summary*; EPA/600/R-94/205; Dallas, Texas, November 30−December 2, 1993.
(7) Lakhtakia, A.; Messier, R. M. *Sculptured Thin Films: Nanoengineered Morphology and Optics*; SPIE: Bellingham, WA, 2005.
(8) Pursel, S.; Horn, M. W.; Demirel, M. C.; Lakhtakia, A. Growth of sculptured polymer submicronwire assemblies by vapor deposition. *Polymer* **2005**, *46*, 9544−9548.
(9) Horn, M. W.; Pickett, M. D.; Messier, R.; Lakhtakia, A. Blending of nanoscale and microscale in uniform large-area sculptured thin-film architectures. *Nanotechnology* **2004**, *15*, 303−310.
(10) Horn, M. W.; Pickett, M. D.; Messier, R.; Lakhtakia, A. Selective growth of sculptured nanowires on microlithographic substrates. *J. Vac. Sci. Technol. B* **2004**, *22*, 3426−3430.
(11) Lakhtakia, A.; McCall, M. W.; Sherwin, J. A.; Wu, Q. H.; Hodgkinson, I. J. Sculptured-thin-film spectral holes for optical sensing of fluids. *Opt. Commun.* **2001**, *194*, 33−46.
(12) DOE, Natural and Accelerated Bioremediation Research Program, Office of Biological and Environmental Research, Office of Science. *Bioremediation of Metal and Radionuclides...What it is and how it works;* LBNL − 42595; 2003.
(13) Lower, S. K.; Hochella, M. F.; Banfield, J. F. Nanogeoscience: from the movement of electrons to lithospheric plates. *EOS* **2002**, *83*, 53−56.
(14) Gilbert, B.; Huang, F.; Zhang, H.; Banfield, J. F. Nanoparticles: strained and stiff. *Science* **2004**, *305*, 651−654.
(15) Rauscher, M.; Hopkins, J. Grazing incidence small-angle X-ray scattering from free-standing nanostructures. *J. Appl. Phys.* **1999**, *86*, 6763−6769.
(16) Schmidbauer, M.; Grigoriev, D.; Hanke, M.; Schafer, P.; Wiebach, T.; Kohler, R. Effects of grazing incidence conditions on the x-ray diffuse scattering from self-assembled nanoscale islands. *Phys. Rev B* **2005**, *71*, 115324.
(17) Levine, J. R.; Cohen, L. B.; Chung, Y. W.; Georgopoulos, P. Grazing-incidence small-angle x-ray-scattering − new tool for studying thin-film growth source. *J. Appl. Crystallogr.* **1989**, *22*, 528−532.
(18) Marra, W. C.; Eisenberger, P.; Cho, A. Y. X-ray total-external-reflection-Bragg diffraction: A structural study of the GaAs-Al interface. *J. Appl. Phys.* **1979**, *50*, 6927−6933.
(19) Royer, R. A.; Burgos, W. D.; Fisher, A. S.; Dempsey B. A.; Unz, R. F. Enhancement of biological reduction of hematite by electron shuttling and Fe(II) complexation. *Environ. Sci. Technol.* **2002**, *36*, 1939−1946.
(20) Parratt, L. G. Surface studies of solids by total reflection of x-rays. *Phys. Rev.* **1954**, *95*, 359−369
(21) D'Acapito, F.; Zontone, F. Grazing-incidence X-ray diffraction in the study of metallic clusters buried in glass obtained by ion implantation. *J. Appl. Crystallogr.* **1999**, *32*, 234−240.
(22) Okamoto, K.; Hara, K.; Kamiya, M.; Hashimoto, T.; Fujiwara, H. Crystallographic investigation of the iron films deposited obliquely by sputtering. *Thin Solid Films* **1989**, *176*, 255−262.
(23) Lovley, D. R.; Phillips, E. J. P. Novel mode of microbial energy metabolism: organic carbon oxidation coupled to dissimilatory reduction of Fe or manganese. *Appl. Environ. Microbiol.* **1988**, *54*, 1472−1480.
(24) Zachara, J. M.; Fredrickson, J. K.; Li, S. M.; Kennedy, D. W.; Smith, S. C.; Gassman, P. L. Bacterial reduction of crystalline Fe^{3+} oxides in single phase suspensions and subsurface materials. *Am. Mineral.* **1998**, *83*, 1426−1443.
(25) Roden, E. E.; Zachara, J. M. Microbial reduction of crystalline Fe^{3+} oxides: Influence of oxide surface area and potential for cell growth. *Environ. Sci. Technol.* **1996**, *30*, 1618−1628.
(26) Lakhtakia, A.; Horn, M. W. Bragg-regime engineering by columnar thinning of chiral sculptured thin films. *Optik (Jena)* **2003**, *114*, 556−560.

Received for review February 17, 2006. Revised manuscript received June 27, 2006. Accepted July 5, 2006.

ES060388J